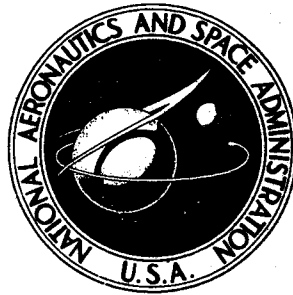


**NASA TECHNICAL  
MEMORANDUM**



**NASA TM X-3417**

**NASA TM X-3417**

**CASE FILE  
COPY**

**HEAT-TRANSFER DISTRIBUTIONS  
ON A 0.013-SCALE SHUTTLE SOLID  
ROCKET BOOSTER AT MACH 3.70 AND  
ANGLES OF ATTACK FROM 0° TO 180°**

*Milton Lamb and Robert L. Stallings, Jr.*

*Langley Research Center*

*Hampton, Va. 23665*



1. Report No. NASA TM X-3417		2. Government Accession No.		3. Recipient's Catalog No.	
4. Title and Subtitle HEAT-TRANSFER DISTRIBUTIONS ON A 0.013-SCALE SHUTTLE SOLID ROCKET BOOSTER AT MACH 3.70 AND ANGLES OF ATTACK FROM 0° TO 180°.				5. Report Date November 1976	
				6. Performing Organization Code	
7. Author(s) Milton Lamb and Robert L. Stallings, Jr.				8. Performing Organization Report No. L-11011	
				10. Work Unit No. 505-11-41-16	
9. Performing Organization Name and Address  NASA Langley Research Center Hampton, VA 23665				11. Contract or Grant No.	
				13. Type of Report and Period Covered Technical Memorandum	
12. Sponsoring Agency Name and Address  National Aeronautics and Space Administration Washington, DC 20546				14. Sponsoring Agency Code	
15. Supplementary Notes					
16. Abstract <p>An experimental investigation has been conducted in the Langley Unitary Plan wind tunnel to estimate the peak aerodynamic heating on the space shuttle solid rocket booster during the descent phase of its flight. Heat-transfer measurements were obtained using 0.013-scale models instrumented with thermocouples at a Mach number of 3.70, Reynolds number per meter of <math>11.48 \times 10^6</math>, and angles of attack from 0° to 180°. Preliminary trajectory studies for the full-scale booster indicate that peak heating will occur at a Mach number of 3.75 and Reynolds number per meter of approximately <math>2.6 \times 10^6</math>.</p> <p>At angles of attack of 0° and 180°, heat-transfer measurements on the cylindrical section of the model between the conical nose and ring interaction region were in good agreement with flat-plate strip theory for laminar and turbulent flow, respectively. At angles of attack up to 30°, measurements on this section of the model were in good agreement with laminar swept-cylinder theory, whereas at angles of attack from 120° to 180°, the measurements were in good agreement with turbulent swept-cylinder theory. The good agreement with turbulent theory indicated that large flow disturbances created by the nozzle and afterbody flare at these large angles of attack influenced the downstream heating primarily by promoting boundary-layer transition; however, there is little information available concerning the boundary-layer transition at flight conditions. Measurements obtained at 90° angle of attack were indicative of laminar flow.</p> <p>Large heating gradients occurred in the ring and flare interaction regions at all angles of attack with the exception of 90°. Peak heating in these interaction regions occurred at 40° angle of attack.</p>					
17. Key Words (Suggested by Author(s)) Heat-transfer distribution Shuttle solid rocket booster Angles of attack, 0° to 180°			18. Distribution Statement Unclassified - Unlimited  Subject Category 01		
19. Security Classif. (of this report) Unclassified	20. Security Classif. (of this page) Unclassified	21. No. of Pages 31	22. Price* \$3.75		

# HEAT-TRANSFER DISTRIBUTIONS ON A 0.013-SCALE SHUTTLE

## SOLID ROCKET BOOSTER AT MACH 3.70 AND

### ANGLES OF ATTACK FROM 0° TO 180°

Milton Lamb and Robert L. Stallings, Jr.  
Langley Research Center

#### SUMMARY

An experimental investigation has been conducted in the Langley Unitary Plan wind tunnel to estimate the peak aerodynamic heating on the space shuttle solid rocket booster during the descent phase of its flight. Heat-transfer measurements were obtained using 0.013-scale models instrumented with thermocouples at a Mach number of 3.70, Reynolds number per meter of  $11.48 \times 10^6$ , and angles of attack from 0° to 180°. Preliminary trajectory studies for the full-scale booster indicate that peak heating will occur at a Mach number of 3.75 and Reynolds number per meter of approximately  $2.6 \times 10^6$ .

At angles of attack of 0° and 180°, heat-transfer measurements on the cylindrical section of the model between the conical nose and ring interaction region were in good agreement with flat-plate strip theory for laminar and turbulent flow, respectively. At angles of attack up to 30°, measurements on this section of the model were in good agreement with laminar swept-cylinder theory, whereas at angles of attack from 120° to 180°, the measurements were in good agreement with turbulent swept-cylinder theory. The good agreement with turbulent theory indicated that large flow disturbances created by the nozzle and afterbody flare at these large angles of attack influenced the downstream heating primarily by promoting boundary-layer transition; however, there is little information available concerning the boundary-layer transition at flight conditions. Measurements obtained at 90° angle of attack were indicative of laminar flow.

Large heating gradients occurred in the ring and flare interaction regions at all angles of attack with the exception of 90°. Peak heating in these interaction regions occurred at 40° angle of attack.

## INTRODUCTION

The space shuttle solid rocket booster after separation from the shuttle has no active aerodynamic control and descends with a tumbling motion. Because of the random orientation during this tumbling descent, angles of attack can occur from  $0^\circ$  to  $180^\circ$ . Some of the problems associated with this wide variation in angle of attack are defining the peak aerodynamic heating that the booster will encounter and specifying a thermal protection system that will permit recovery and reuse of the booster. Although there is considerable information in the literature that can be used for predicting the heating on a basic shape at small angles of attack, very little data exist that can be applied to the solid rocket booster for the full range of angles up to  $180^\circ$ .

In order to provide some insight into this problem, an experimental heat-transfer investigation was conducted in the Langley Unitary Plan wind tunnel using 0.013-scale models of the shuttle solid rocket booster at angles of attack from  $0^\circ$  to  $180^\circ$ . The models consisted of a blunted  $18^\circ$  conical nose section, a cylindrical body section approximately 10 diameters in length, a flared afterbody, and a conical exhaust nozzle. The tests were conducted at a Mach number of 3.70 and a Reynolds number per meter of  $11.48 \times 10^6$ . Preliminary trajectory studies for the full-scale booster indicate that peak heating will occur at a Mach number of 3.75 and Reynolds number per meter of approximately  $2.6 \times 10^6$ .

## SYMBOLS

b	local skin thickness, cm
c	specific heat of model skin, J/kg-K
$c_p$	specific heat of air at constant pressure, J/kg-K
h	heat-transfer coefficient, J/m <sup>2</sup> -sec-K
l	configuration length, cm
$N_{St}$	Stanton number based on free-stream conditions
r	radius, cm
T	temperature, K
$T_e$	measured wall temperature at steady-state conditions, K



$T_t$         stagnation temperature, K  
 $T_w$         wall temperature, K  
 $t$            time, sec  
 $V_\infty$        free-stream velocity, m/sec  
 $x$            axial length, measured from tip of nose, cm  
 $\alpha$           angle of attack, deg  
 $\theta$           polar angle (see fig. 1), deg  
 $\rho$            density of model skin, kg/m<sup>3</sup>  
 $\rho_\infty$         density of air at free-stream conditions, kg/m<sup>3</sup>

Subscripts:

0, 1, ..., n        time sequence

## APPARATUS AND TEST CONDITIONS

This investigation was conducted in the high Mach number test section of the Langley Unitary Plan wind tunnel described in reference 1. It is a variable-pressure, continuous-flow tunnel with an asymmetrical sliding-block nozzle that permits a continuous variation in the test-section Mach number from 2.30 to 4.65. For the present investigation the heat-transfer measurements were made at a Mach number of 3.70 and at Reynolds number per meter of  $11.48 \times 10^6$ .

## MODELS AND INSTRUMENTATION

The models used in this investigation consisted of a blunted 18° conical nose section, a cylindrical body section approximately 10 diameters in length, a flared afterbody, and a conical exhaust nozzle. The models had a thin skin with an average thickness of 0.00762 cm and each was instrumented with approximately 118 iron-constantan thermocouples. Also, in order to minimize the effects of the sting on the model flow field throughout the large angle-of-attack range, three different models having different sting installations were tested. The thermocouple locations and sting arrangements are shown in figure 1 for models A, B, and C. Photographs of the models installed in the tunnel are shown in figure 2.

The thermocouple outputs were amplified, digitized, and magnetically recorded at 1/2-sec intervals for 14 sec by a high-speed analog-digital recording system.

The free-stream stagnation pressure was measured on a precision mercury manometer. The test-section stagnation temperature was measured with double-shielded stagnation-temperature probes attached to the vertical wall of the test section external to the sidewall boundary layer and located at the same longitudinal location as the model.

## METHOD OF HEAT-TRANSFER DATA REDUCTION

The heat-transfer coefficients were obtained from transient skin-temperature measurements resulting from a stepwise increase in stagnation temperature. This technique is described in detail in reference 2.

The heat-balance equation reduces to

$$h = \frac{\rho bc \frac{dT_w}{dt}}{T_e - T_w} \quad (1)$$

when it is assumed there is negligible lateral heat flow, constant temperature through the model skin, negligible heat flow to the model interior, and no heat losses due to radiation.

This equation can be integrated and written in the following form for complete machine calculation:

$$h = \frac{\rho bc (T_{w,n} - T_{w,o})}{\frac{T_e}{T_t} \int_0^t T_t dt - \int_0^t T_w dt} \quad (2)$$

The integrals of equation (2) were evaluated using the trapezoidal rule, and the ratio  $T_e/T_t$  was experimentally determined (ref. 2). The heat-transfer coefficients were converted to Stanton numbers using the following equation:

$$N_{St} = \frac{h}{\rho_{\infty} V_{\infty} c_p} \quad (3)$$

## RESULTS AND DISCUSSION

Typical schlieren photographs for angles of attack ranging from  $0^\circ$  to  $180^\circ$  are presented in figure 3. Complicated flow fields consisting of intersecting shock waves, shear layers, and separation regions are visible in these photographs, especially in the vicinity of the ring and afterbody flare at the higher angles of attack.

Stagnation-line heating distributions for the conical nose and cylindrical portion of the models ahead of the ring ( $x/r_1 < 0.6$ ) are presented in figure 4 for angles of attack from  $0^\circ$  and  $180^\circ$ . For angles of attack of  $0^\circ$  and  $180^\circ$ , the measured heating distributions are compared with flat-plate strip theory based on the method of reference 3. At  $\alpha = 0^\circ$  the strip theory for the conical nose was calculated using local conditions for a sharp cone, whereas for the cylindrical section local conditions were assumed equal to free-stream values. Local Reynolds numbers for both sections of the model were based on the axial distance from the cone nose tip. At  $\alpha = 180^\circ$  theoretical heating distributions were calculated for only the cylindrical section of the model. These calculations were based on free-stream static pressures, a local total pressure corresponding to the total pressure behind a normal shock, and a local Reynolds number based on axial distance from the nozzle base ( $x/r_1 = 1.0$ ). For both  $\alpha = 0^\circ$  and  $180^\circ$ , the theoretical Stanton numbers were converted to free-stream values for comparison with the data presented in figure 4.

At  $\alpha = 0^\circ$  the good agreement between measured heating rates and that predicted by laminar strip theory (fig. 4(a)) suggests that laminar flow prevails over the model for  $x/r_1 < 0.6$ . At  $\alpha = 180^\circ$  the fair agreement between experimental data and the data obtained from turbulent strip theory for this region (fig. 4(b)) suggests that the turbulence induced by the complex flow over the nozzle, afterbody flare, and circumferential ring results in a fully turbulent boundary layer for  $x/r_1 < 0.6$ . It is interesting to note that these large upstream disturbances did not result in heating rates that were larger than turbulent flat-plate values for  $x/r_1 < 0.6$ .

The effect of angle of attack on the stagnation-line heating rates, as shown in figures 4(a) and 4(b), consists of an

increase in heating with increasing angle of attack through  $\alpha = 75^\circ$ , a decrease in heating with increasing  $\alpha$  from  $75^\circ$  to  $105^\circ$ , an increase in heating with increasing  $\alpha$  from  $105^\circ$  to  $120^\circ$ , and a decrease in heating with increasing  $\alpha$  from  $120^\circ$  to  $180^\circ$ . In order to show more clearly the variation of the cylindrical-section stagnation-line heating rates with angle of attack, the measured values ( $0.1 < x/r < 0.6$ ) were averaged at each angle of attack and were cross-plotted as a function of angle of attack in figure 5. The variation of the averaged heating rates with angle of attack is not an explicit angle-of-attack effect since part of this variation is caused by transition to turbulent flow occurring at the intermediate angles of attack between  $0^\circ$  and  $90^\circ$  and between  $90^\circ$  and  $180^\circ$ . This transition to turbulent flow is due to either the inherent instability of the three-dimensional boundary layer at those intermediate angles or the upstream contamination induced by the model components. For  $0^\circ < \alpha < 90^\circ$  this contamination could result from an interaction between the flow fields over the conical nose and cylindrical body, and for  $90^\circ < \alpha \leq 180^\circ$  from the complex flow over the model afterbody. As the angle of attack approaches  $90^\circ$ , the flow over the cylindrical section should be laminar since the model end effects are minimized and the boundary layer over the cylindrical section is essentially two-dimensional. Both laminar and turbulent theoretical swept-cylinder heating rates were calculated using the method of reference 4 in an attempt to establish whether the experimental measurements are representative of laminar or turbulent flow. (See fig. 5.) For  $0^\circ < \alpha \leq 30^\circ$  the measurements are generally in good agreement with laminar theory, and for  $140^\circ \leq \alpha \leq 180^\circ$  the measurements are representative of turbulent flow. The magnitude of the experimental heating rates at the other angles of attack suggests that transitional or turbulent flow occurs at  $\alpha = 120^\circ$  and  $40^\circ \leq \alpha \leq 75^\circ$ , and laminar flow occurs at  $\alpha = 90^\circ$  and  $105^\circ$ .

Measured stagnation-line heating distributions in regions of the ring and afterbody flare are presented in figure 6 for the test range of angle of attack. Heating distributions in these regions are influenced not only by the complicated flow interactions created by these model components but also by boundary-layer transition induced by flow disturbances created by these components. Peak heating ahead of the circumferential ring and on the afterbody flare occurs at an angle of attack of  $40^\circ$  and probably in either a transitional or turbulent boundary layer. Increasing the angle of attack to  $90^\circ$  results in a decrease in the peak heating values, and at  $\alpha = 90^\circ$  the stagnation-line heating rate is relatively constant and approximately equal to the apparently laminar stagnation-line values obtained for the cylindrical section at  $\alpha = 90^\circ$ . (See fig. 4.) Further increases in angle of attack up to  $\alpha = 180^\circ$  result in large stagnation-line heating gradients; however, the peak heating values are less than those measured at  $\alpha = 40^\circ$ .

Circumferential heating distributions for various  $x/l$  locations are shown in figure 7. These distributions are typical for a body of revolution at angle of attack consisting of large heating rates on the windward side of the model ( $0^\circ \leq \theta \leq 90^\circ$ ) and reduced heating rates on the leeward side ( $90^\circ \leq \theta \leq 180^\circ$ ). This trend occurs even in flow interaction regions which have large heating gradients at the stagnation line, for example, at  $x/l = 0.7467$  and  $\alpha = 40^\circ$  (fig. 7(a)). The adverse heating gradients occurring at  $\theta = 180^\circ$  for some longitudinal stations are probably due to either lee-surface vortex impingement or boundary-layer transition. The large circumferential heating gradient obtained at  $\alpha = 0^\circ$  and  $x/l = 0.4317$  (fig. 7(a)) is believed to be a result of boundary-layer transition presumably induced by a model surface imperfection located upstream of this station. Unfortunately, the model was not available for inspection at the time this effect was discovered.

### CONCLUDING REMARKS

An experimental investigation has been conducted in the Langley Unitary Plan wind tunnel to estimate the peak aerodynamic heating on the space shuttle solid rocket booster during the descent phase of its flight. Heat-transfer measurements were obtained using 0.013-scale models instrumented with thermocouples at a Mach number of 3.70, Reynolds number per meter of  $11.48 \times 10^6$ , and angles of attack from  $0^\circ$  to  $180^\circ$ . Preliminary trajectory studies for the full-scale booster indicate that peak heating will occur at a Mach number of 3.75 and Reynolds number per meter of approximately  $2.6 \times 10^6$ .

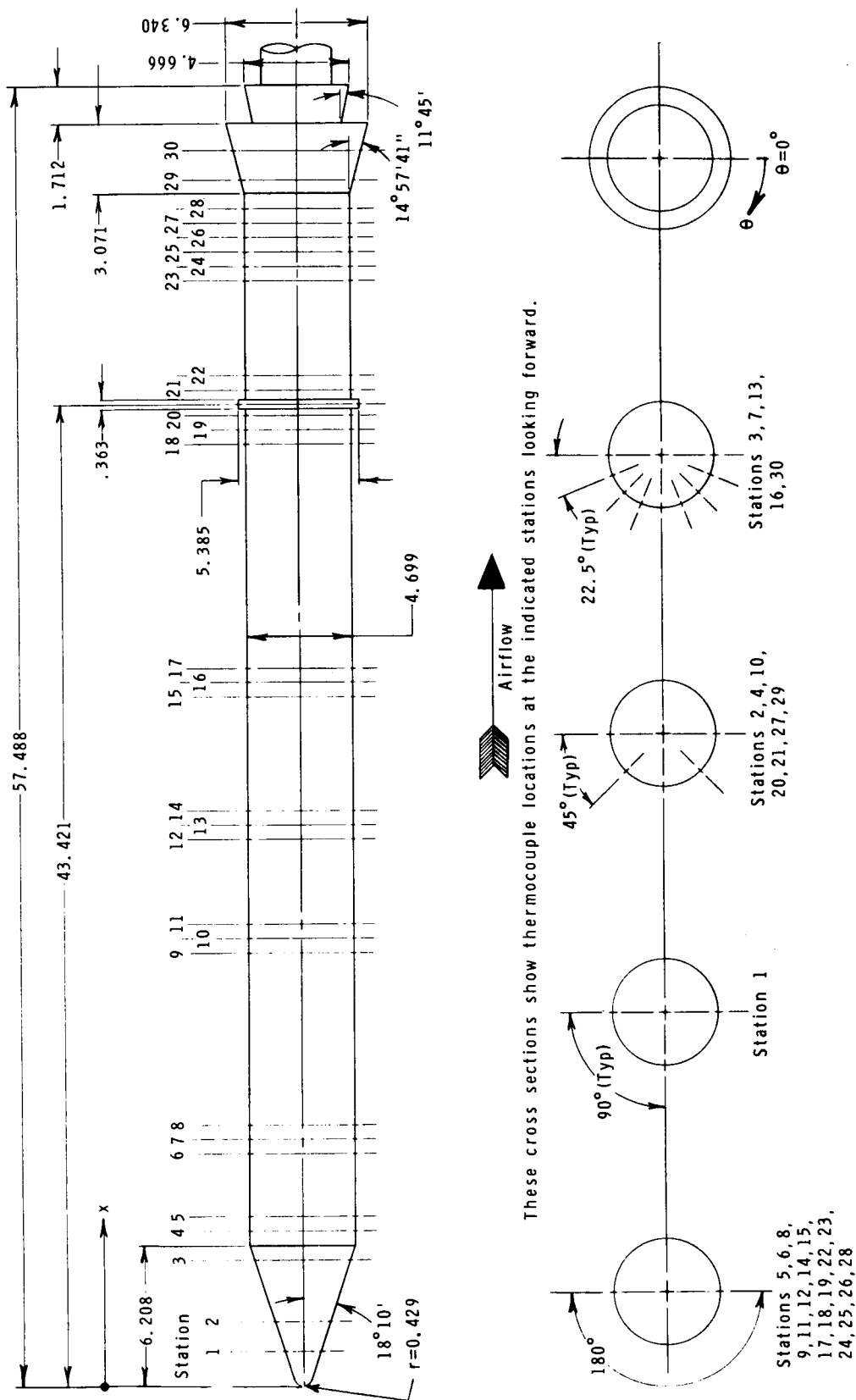
At angles of attack of  $0^\circ$  and  $180^\circ$ , heat-transfer measurements on the cylindrical section of the model between the conical nose and ring interaction region were in good agreement with flat-plate strip theory for laminar and turbulent flow, respectively. At angles of attack up to  $30^\circ$ , measurements on this section of the model were in good agreement with laminar swept-cylinder theory, whereas at angles of attack from  $120^\circ$  to  $180^\circ$  the measurements were in good agreement with turbulent swept-cylinder theory. The good agreement with turbulent theory indicates that large flow disturbances created by the nozzle and afterbody flare at these larger angles of attack influenced the downstream heating primarily by promoting boundary-layer transition; however, there is little information available concerning the boundary-layer transition at flight conditions. Measurements obtained at  $90^\circ$  angle of attack were indicative of laminar flow.

Large heating gradients occurred in the ring and flare interaction regions at all angles of attack with the exception of  $90^\circ$ . Peak heating in these interaction regions occurred at  $40^\circ$  angle of attack.

Langley Research Center  
National Aeronautics and Space Administration  
Hampton, VA 23665  
August 23, 1976

## REFERENCES

1. Manual for Users of the Unitary Plan Wind Tunnel Facilities of the National Advisory Committee for Aeronautics. NACA, 1956.
2. Burbank, Paige B.; and Hodge, B. Leon: Distribution of Heat Transfer on a  $10^\circ$  Cone at Angles of Attack From  $0^\circ$  to  $15^\circ$  for Mach Numbers of 2.49 to 4.65 and a Solution to the Heat-Transfer Equation That Permits Complete Machine Calculation. NASA MEMO 6-4-59L, 1959.
3. Van Driest, E. R.: Investigation of Laminar Boundary Layer in Compressible Fluids Using the Crocco Method. NACA TN 2597, 1952.
4. Beckwith, Ivan E.; and Gallagher, James, J.: Local Heat Transfer and Recovery Temperatures on a Yawed Cylinder at a Mach Number of 4.15 and High Reynolds Numbers. NASA TR R-104, 1961.



(a) Model A.

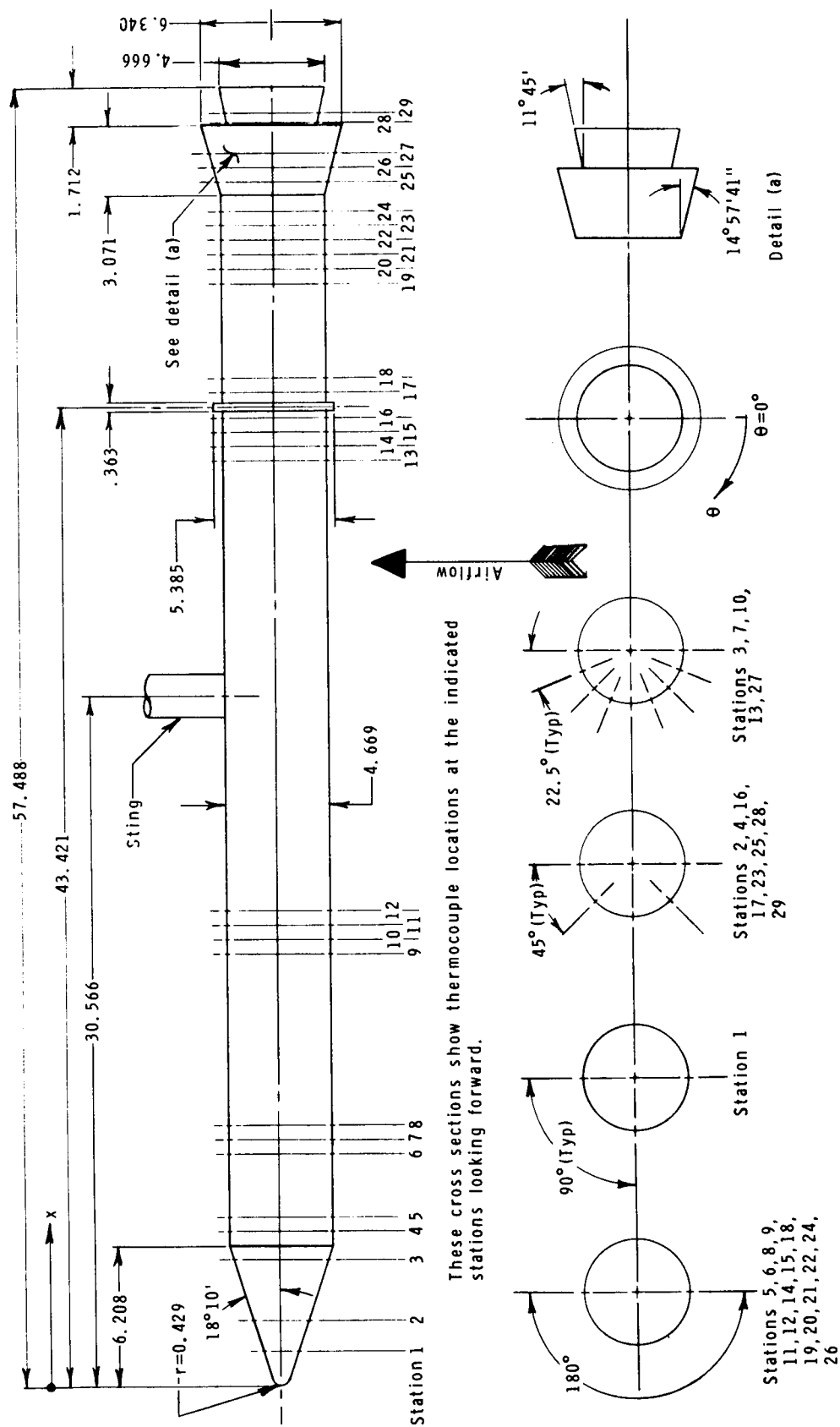
Figure 1.- Drawing of models showing sting arrangement and thermocouple locations.  
All dimensions are in centimeters.



Station	x, cm	Number of thermocouples
1	1.524	3
2	2.845	5
3	5.588	9
4	6.858	5
5	7.493	2
6	10.287	2
7	10.922	9
8	11.557	2
9	19.177	2
10	19.812	5
11	20.447	2
12	24.181	2
13	24.816	9
14	25.451	2
15	30.480	2
16	31.115	9
17	31.750	2
18	41.656	2
19	42.291	2
20	42.926	5
21	44.069	5
22	44.704	2
23	48.895	2
24	49.530	2
25	50.165	2
26	50.800	2
27	51.435	5
28	52.070	2
29	53.340	5
30	54.610	9

(a) Concluded.

Figure 1.- Continued.



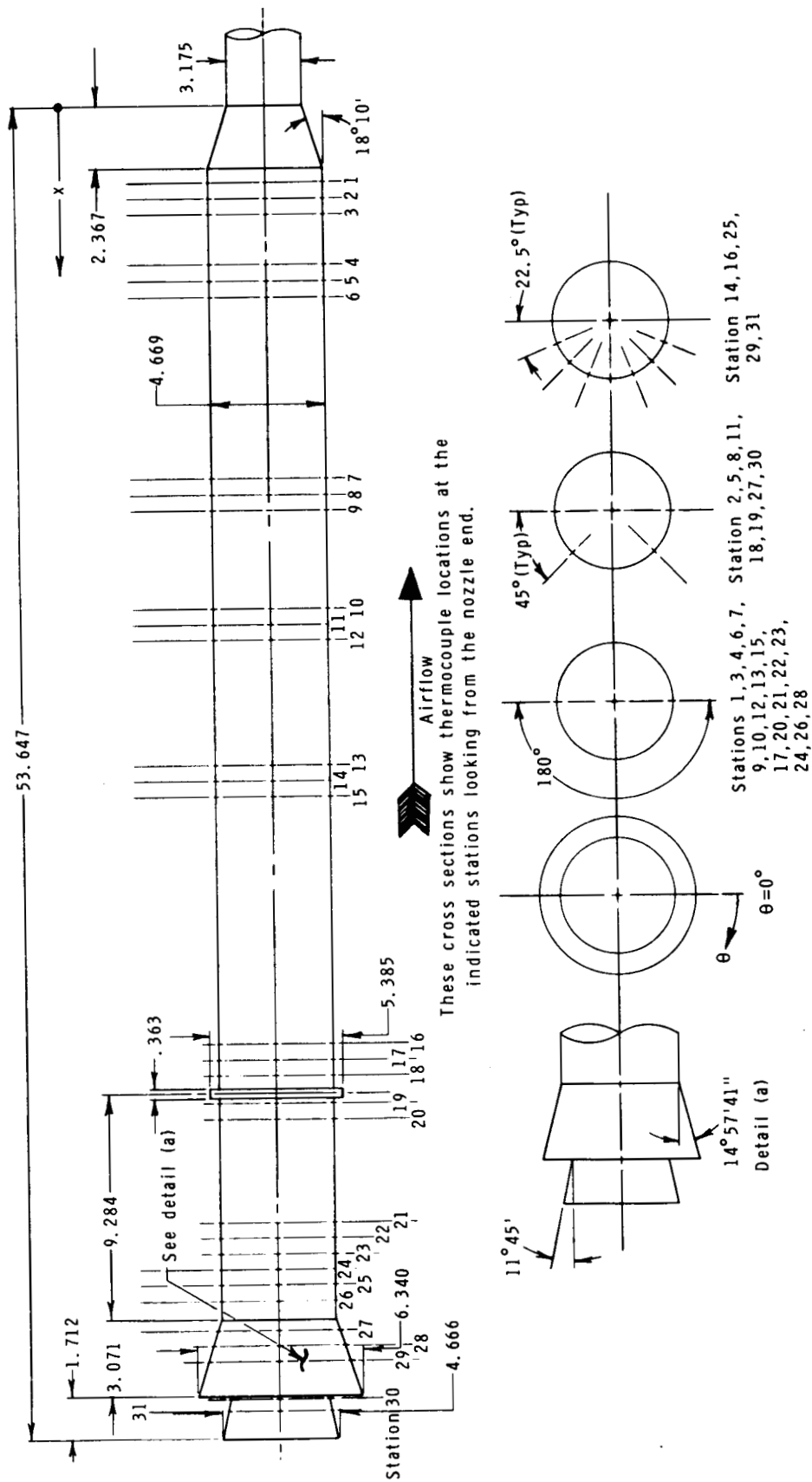
(b) Model B.

Figure 1.- Continued.

Station	x, cm	Number of thermocouples
1	1.524	3
2	2.845	5
3	5.588	9
4	6.858	5
5	7.493	2
6	10.287	2
7	10.922	9
8	11.557	2
9	19.177	2
10	19.812	9
11	20.447	2
12	21.082	2
13	41.021	9
14	41.656	2
15	42.291	2
16	42.926	5
17	44.069	5
18	44.704	2
19	48.895	2
20	49.530	2
21	50.165	2
22	50.800	2
23	51.435	5
24	52.070	2
25	53.340	5
26	53.975	2
27	54.610	9
28	55.865	5
29	56.388	5

(b) Concluded.

Figure 1.- Continued.



(c) Model C.

Figure 1.- Continued.

Station	x, cm	Number of thermocouples
1	3.175	2
2	3.810	5
3	4.445	2
4	6.477	2
5	7.112	5
6	7.747	2
7	15.113	2
8	15.748	5
9	16.383	2
10	20.320	2
11	20.955	5
12	21.590	2
13	26.645	2
14	27.280	9
15	27.915	2
16	37.846	9
17	38.481	2
18	39.116	5
19	40.234	5
20	40.869	2
21	45.060	2
22	45.695	2
23	46.330	2
24	46.965	2
25	47.600	9
26	48.235	2
27	49.428	5
28	50.063	2
29	50.698	9
30	52.070	5
31	52.553	9

(c) Concluded.

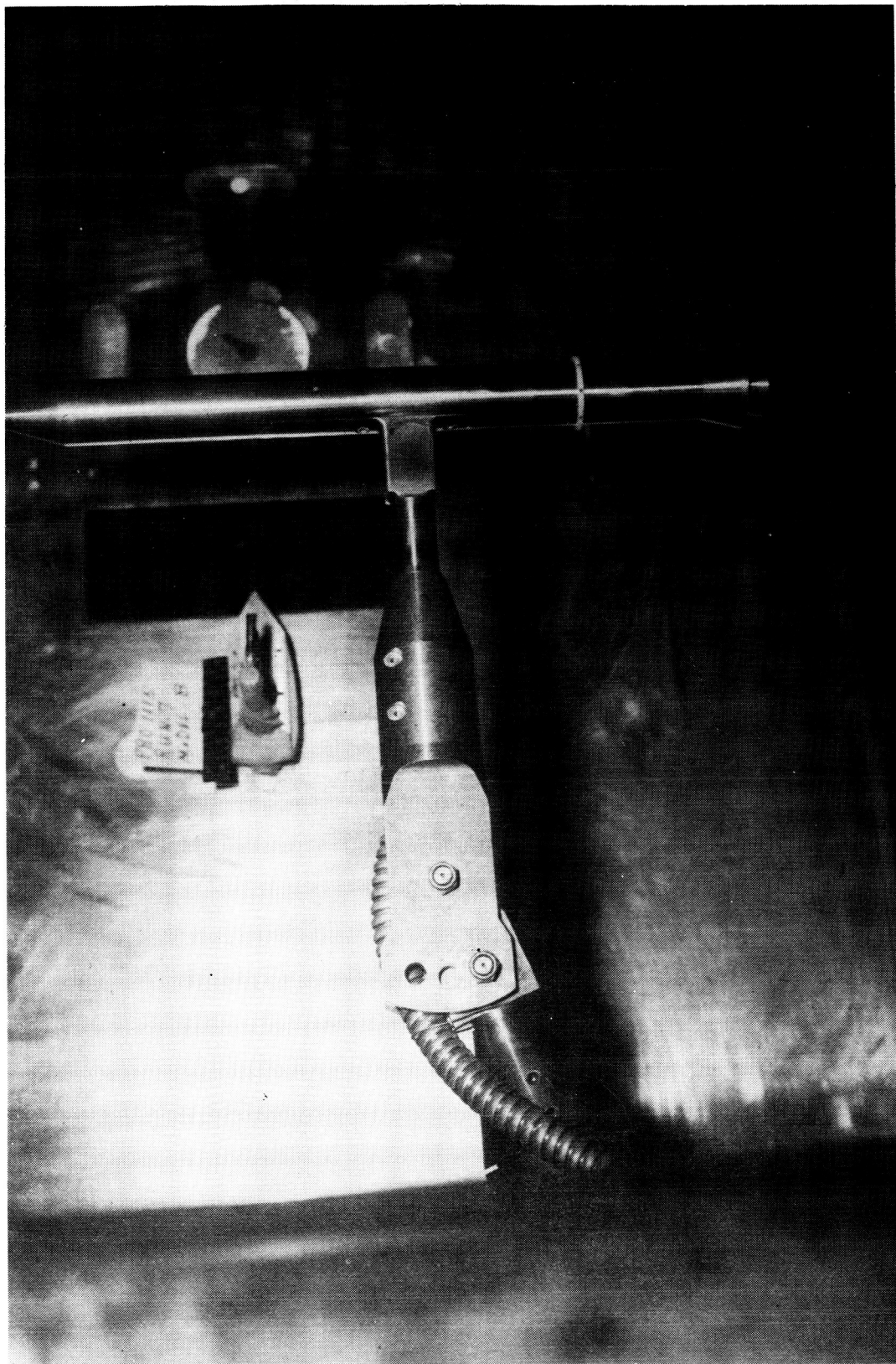
Figure 1.- Concluded.



L-74-6177

(a) Model A.

Figure 2.- Photographs of models in Langley Unitary Plan wind tunnel.



L-74-6146

(b) Model B.

Figure 2.- Continued.

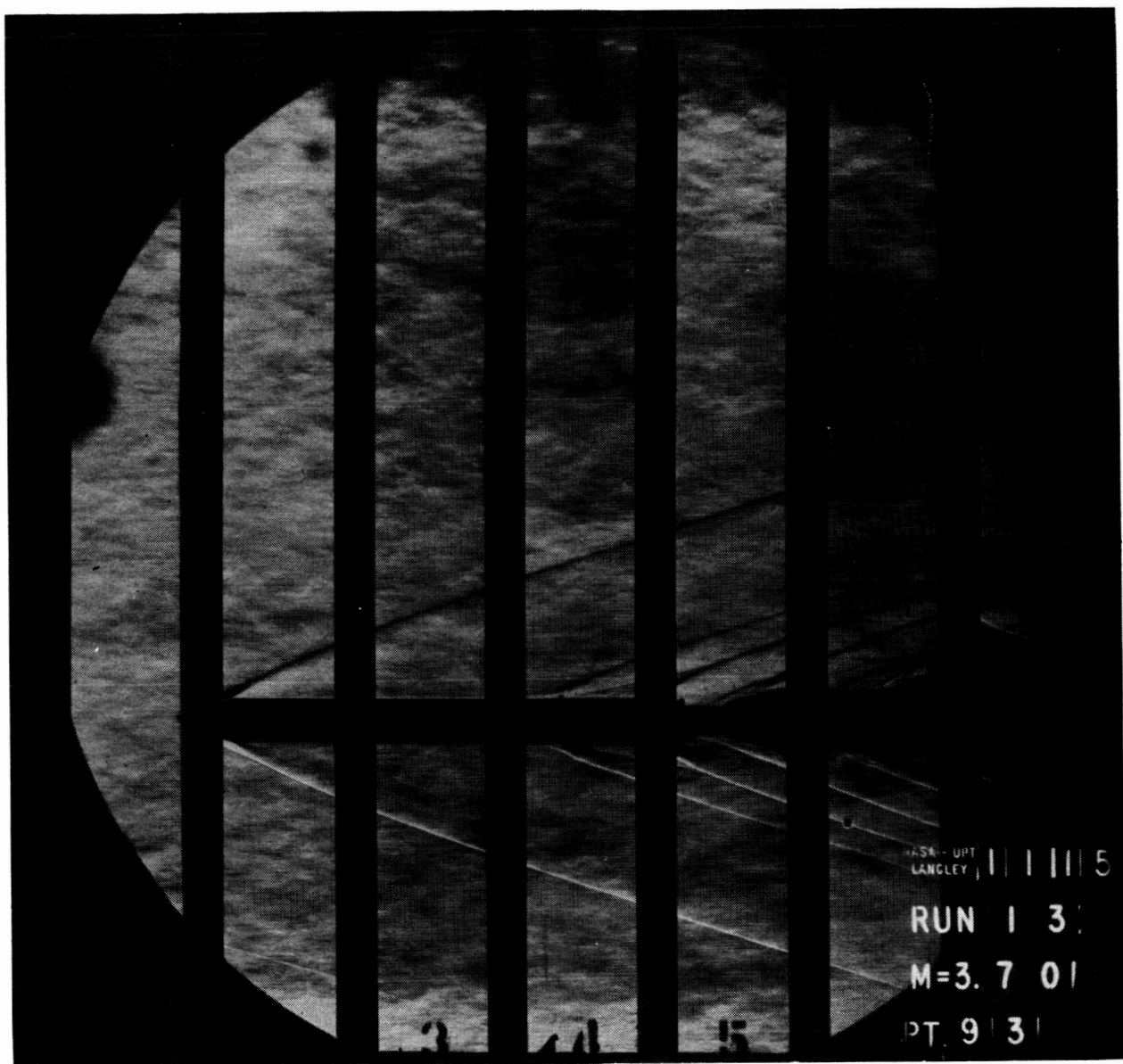


L-74-6170

(c) Model C.

Figure 2.- Concluded.

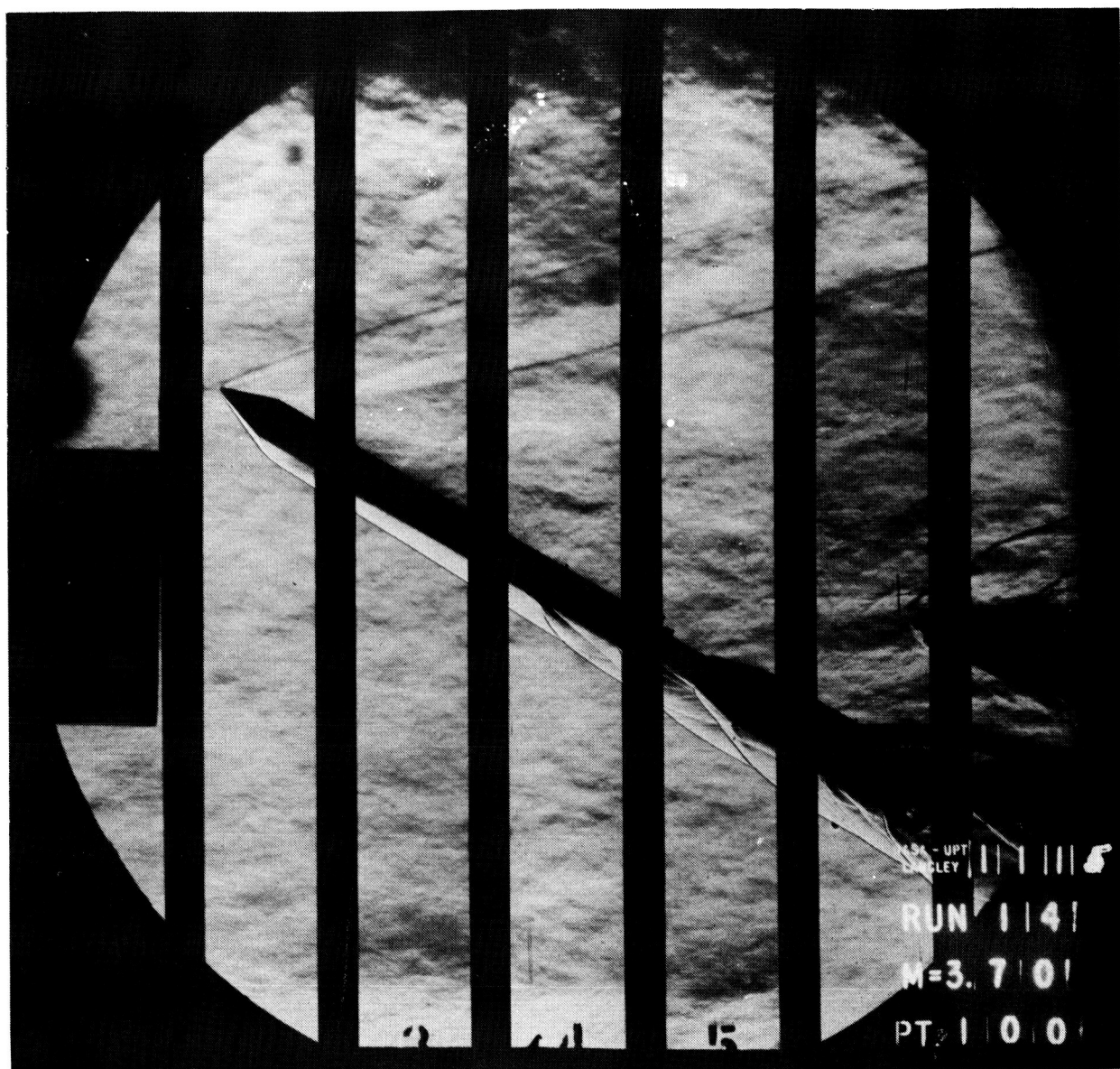




L-76-248

(a)  $\alpha = 0^\circ$ .

Figure 3.- Schlieren photographs.



L-76-249

(b)  $\alpha = 30^\circ$ .

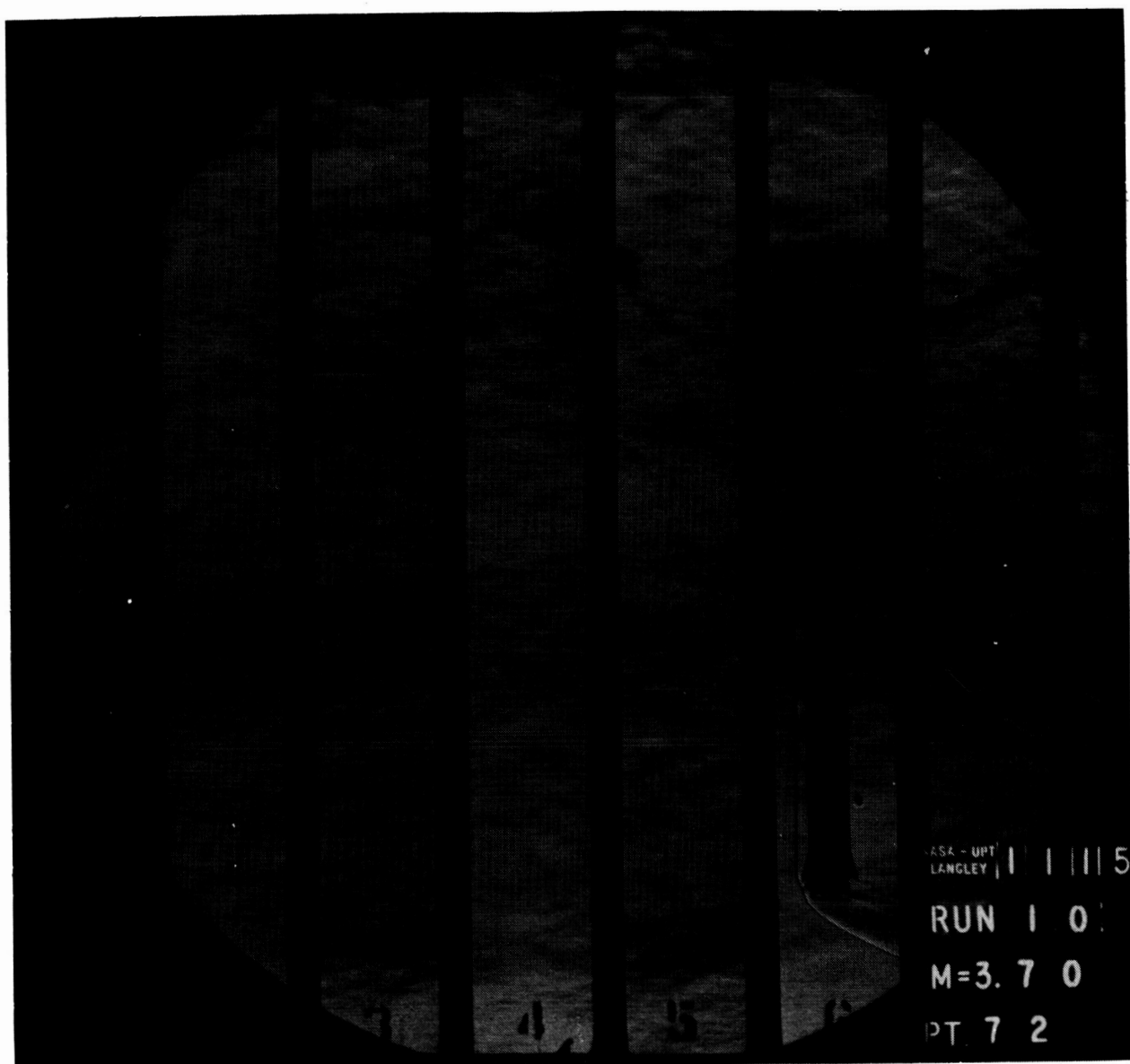
Figure 3.- Continued.



L-76-250

(c)  $\alpha = 60^\circ$ .

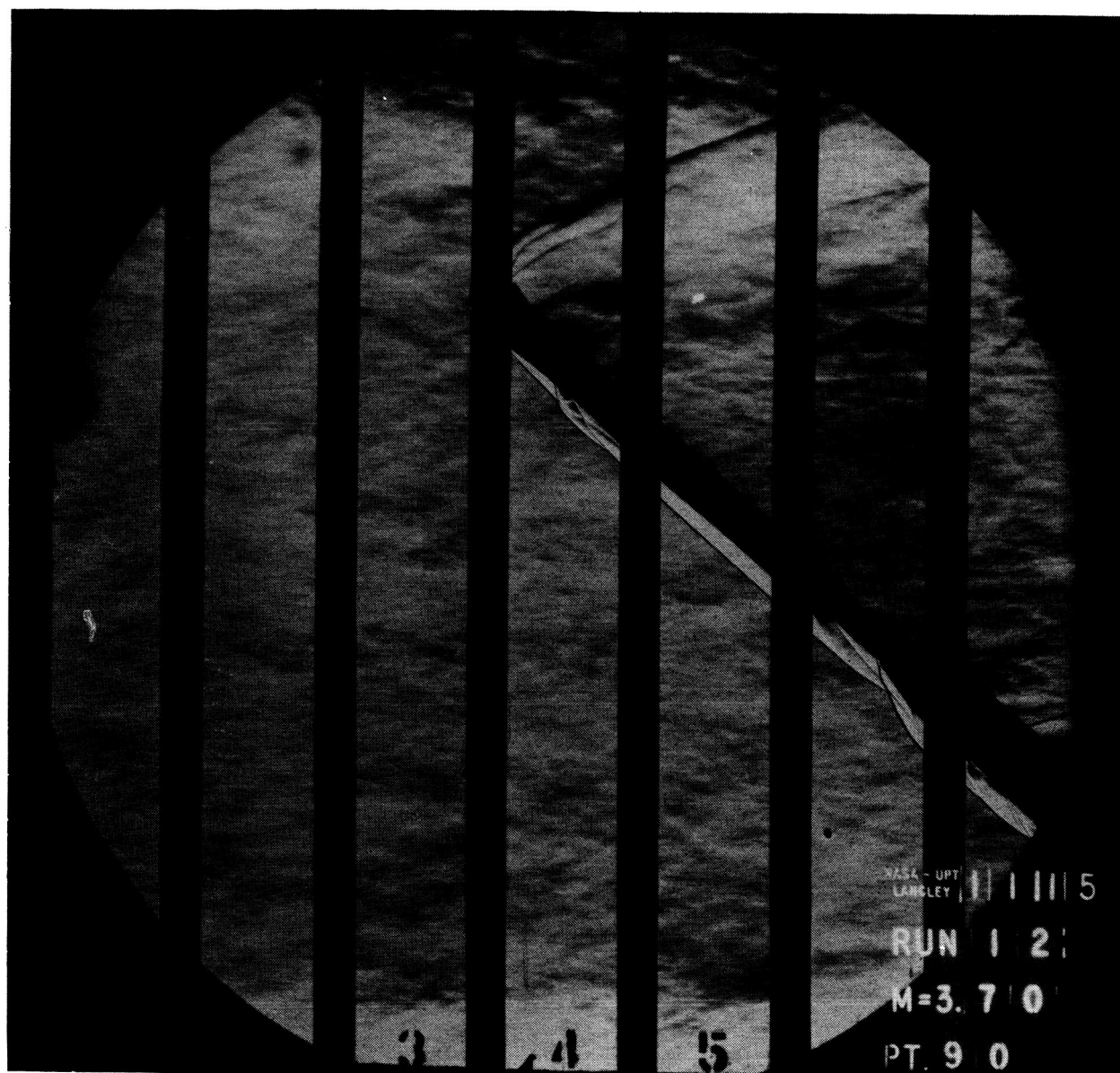
Figure 3.- Continued.



L-76-251

(d)  $\alpha = 90^\circ$ .

Figure 3.- Continued.

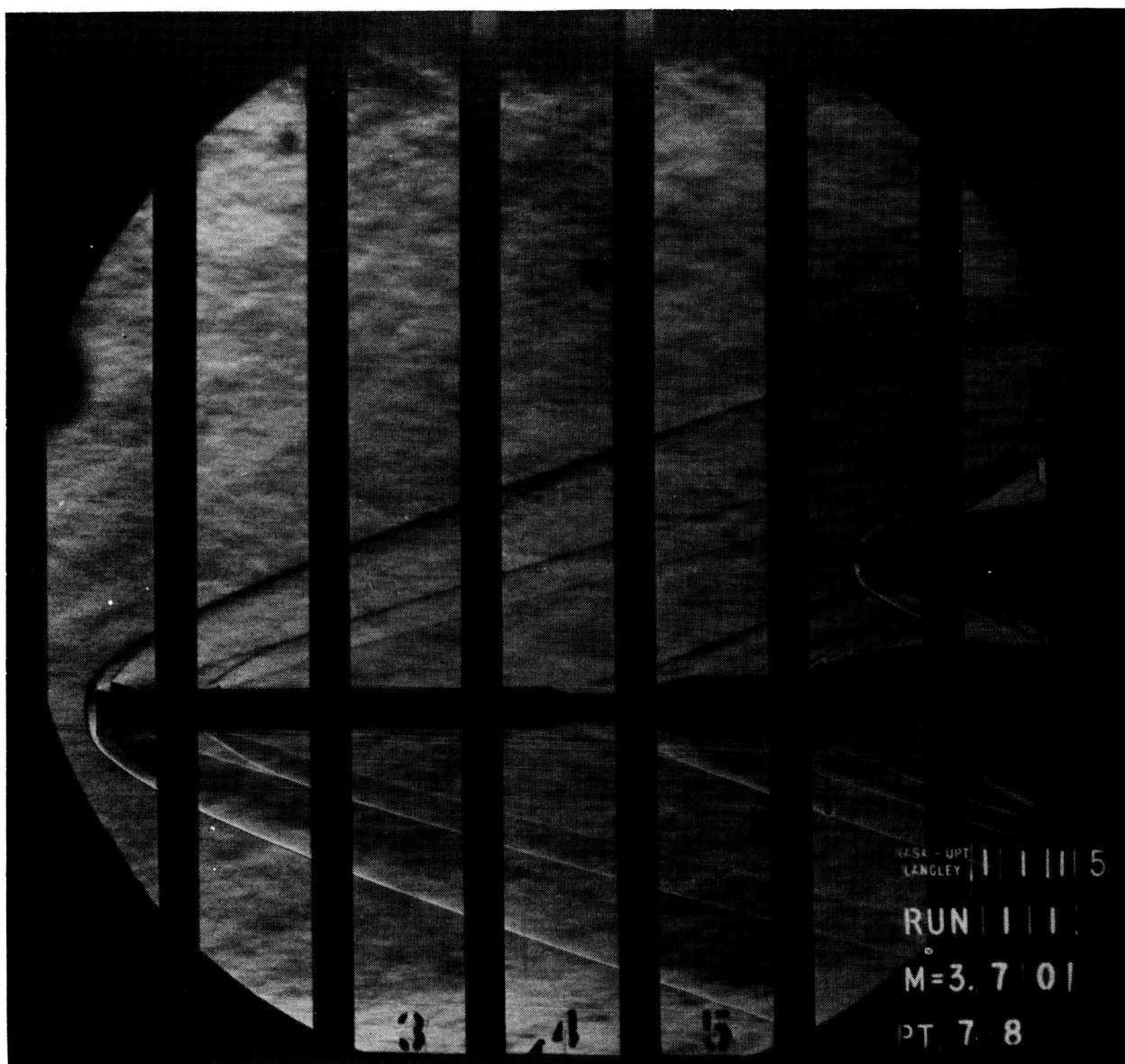


L-76-252

(e)  $\alpha = 140^\circ$ .

Figure 3.- Continued.

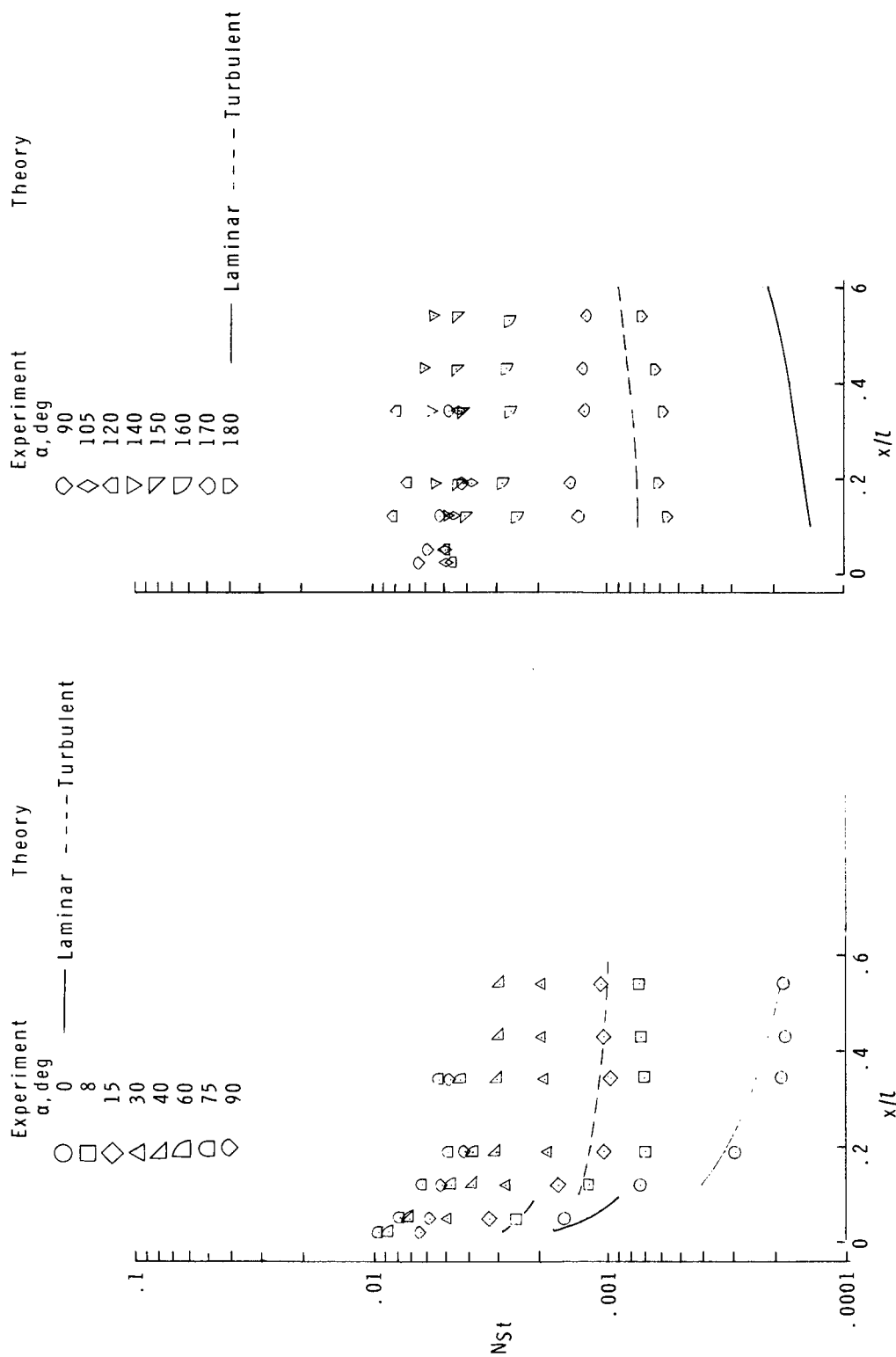




L-76-253

(f)  $\alpha = 180^\circ$ .

Figure 3.- Concluded.



(a)  $0^\circ \leq \alpha \leq 90^\circ$ . (b)  $90^\circ \leq \alpha \leq 180^\circ$ .

Figure 4. Effect of angle of attack on stagnation-line heating distribution,  $x/l < 0.6$ .

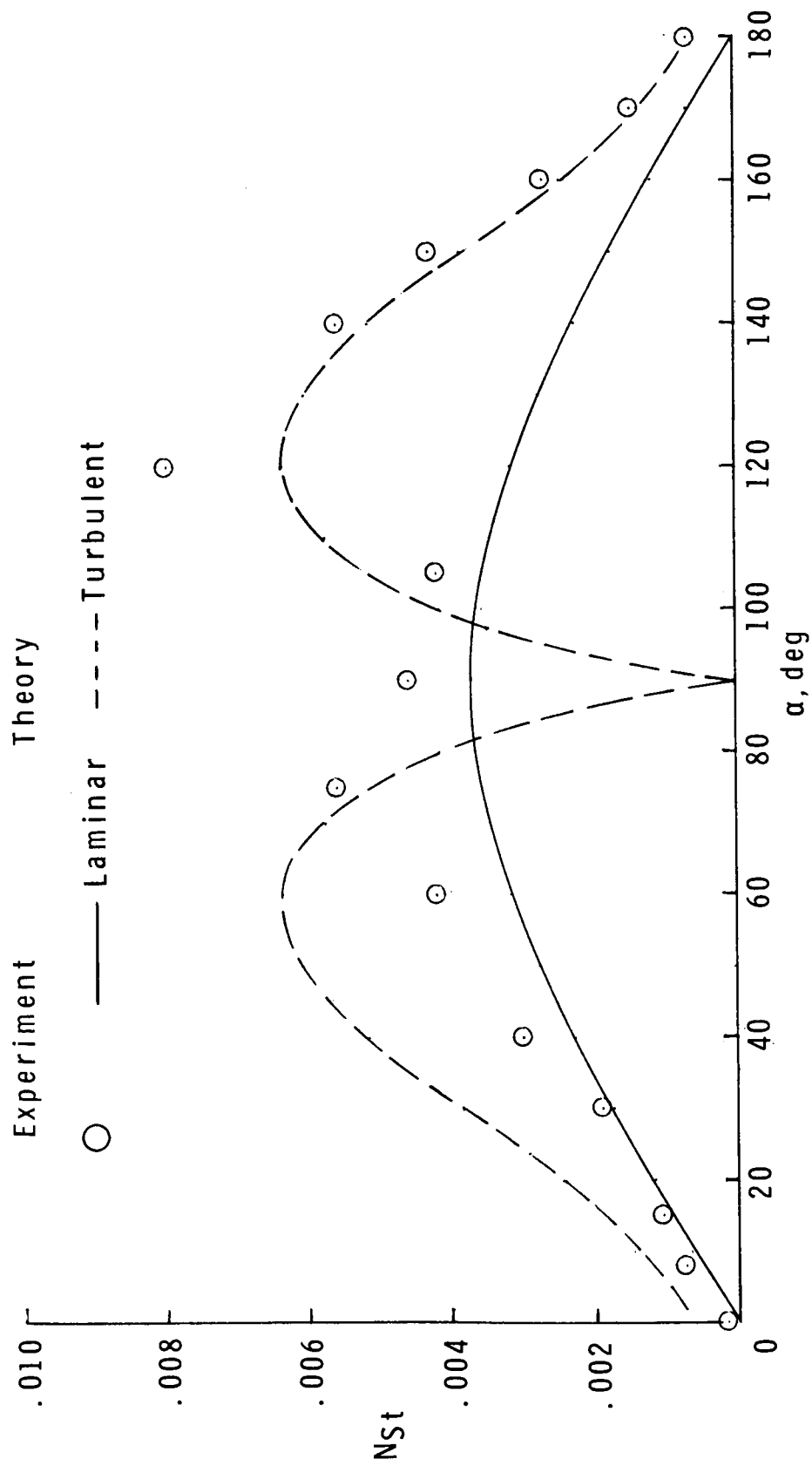
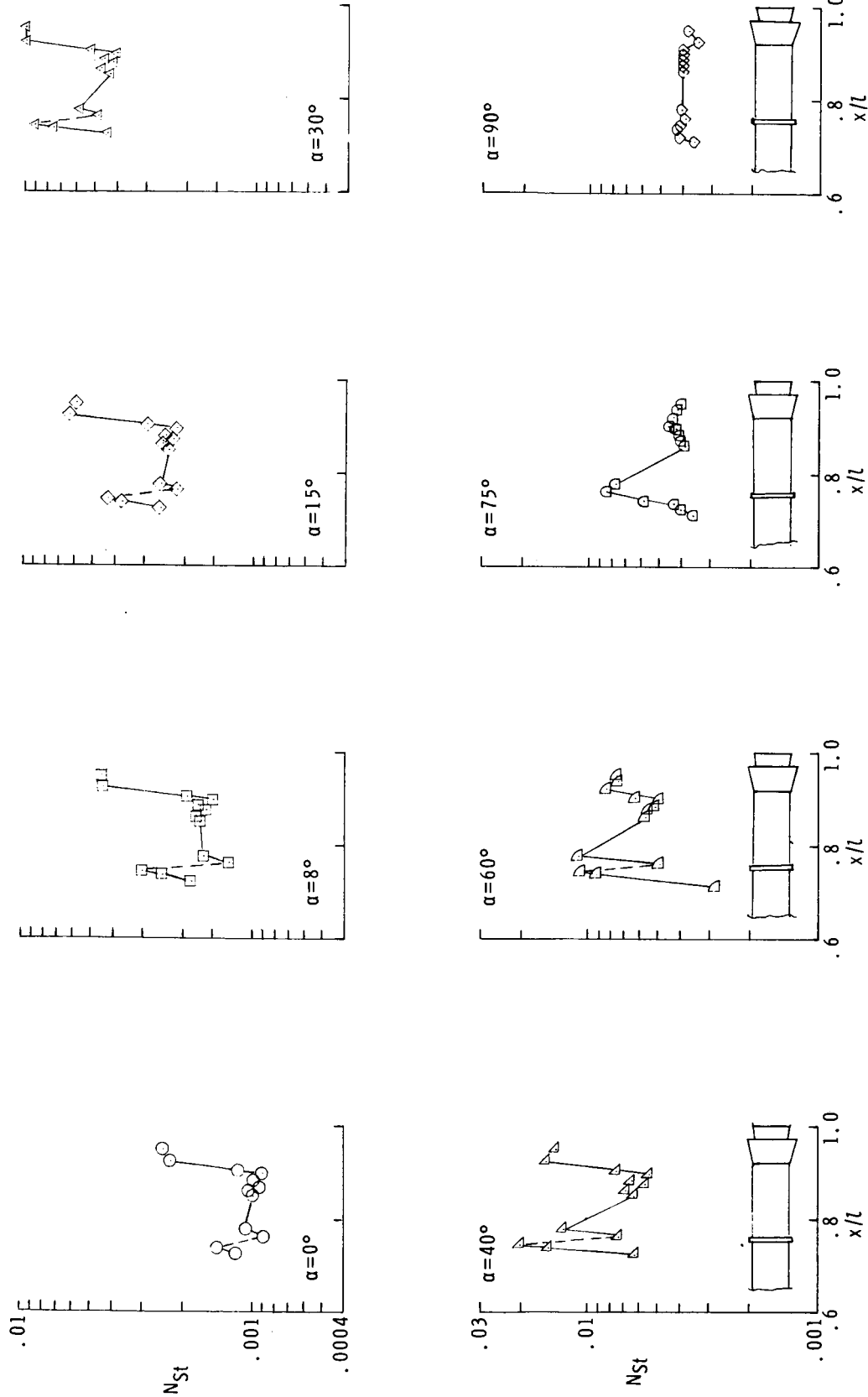


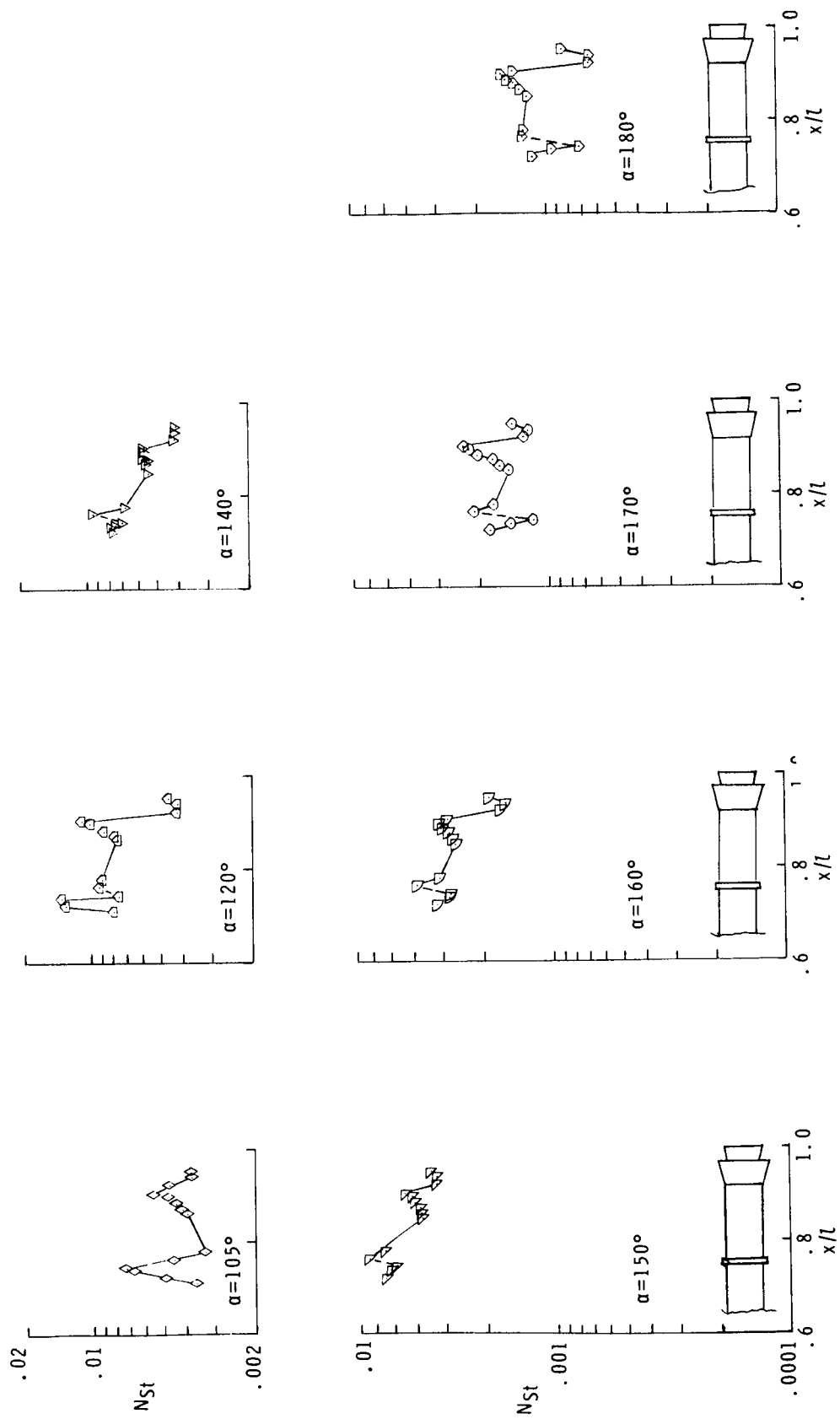
Figure 5.- Comparison of theoretical and average experimental stagnation-line heating rates for the cylindrical section of the model,  $x/l < 0.6$ .





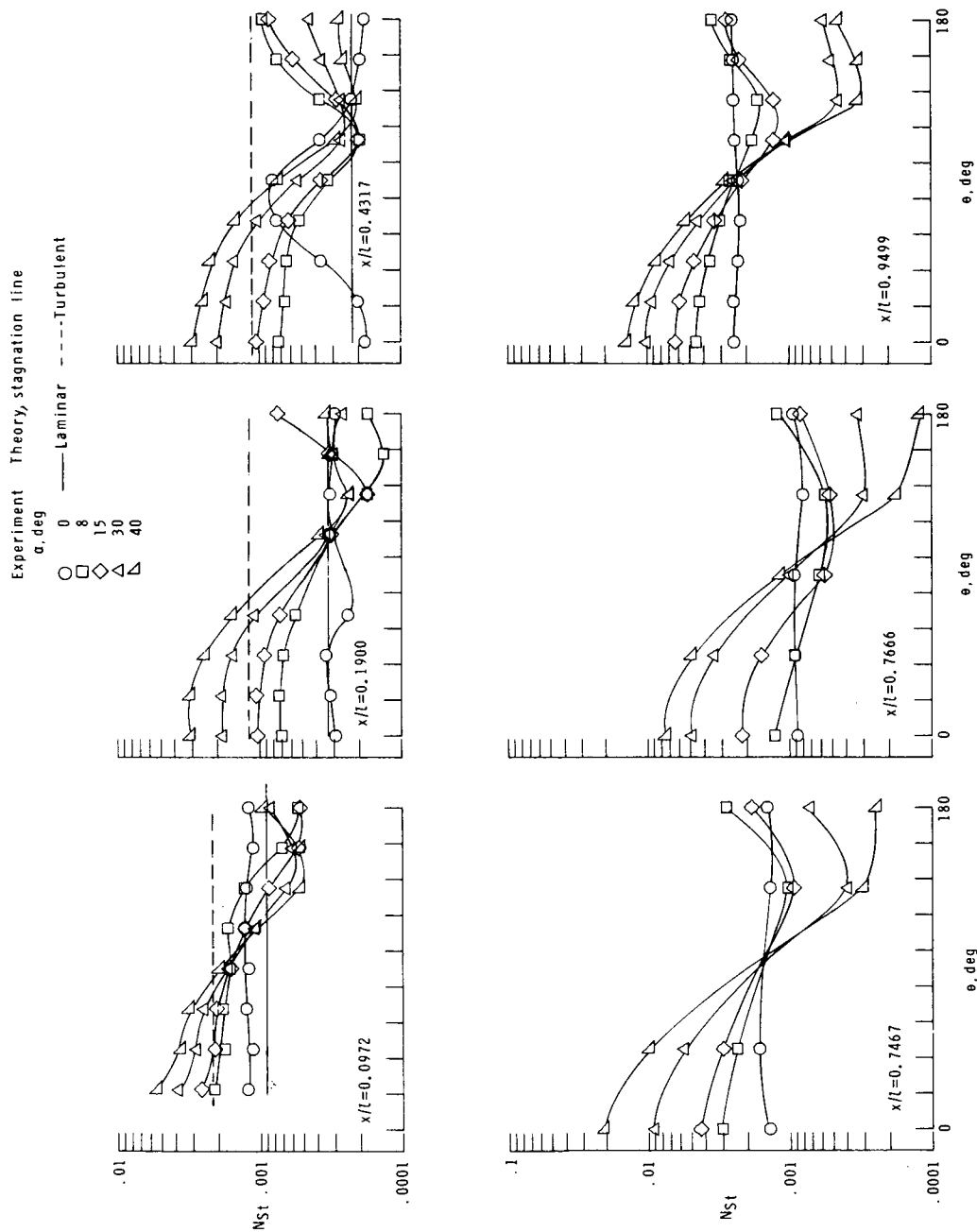
(a)  $0^\circ \leq \alpha \leq 90^\circ$ .

Figure 6.- Effect of angle of attack on stagnation-line heating distribution,  $x/l > 0.6$ .



(b)  $105^\circ \leq \alpha \leq 180^\circ$ .

Figure 6.- Concluded.



(a) Model A.

Figure 7.- Effect of angle of attack on circumferential heating distribution.

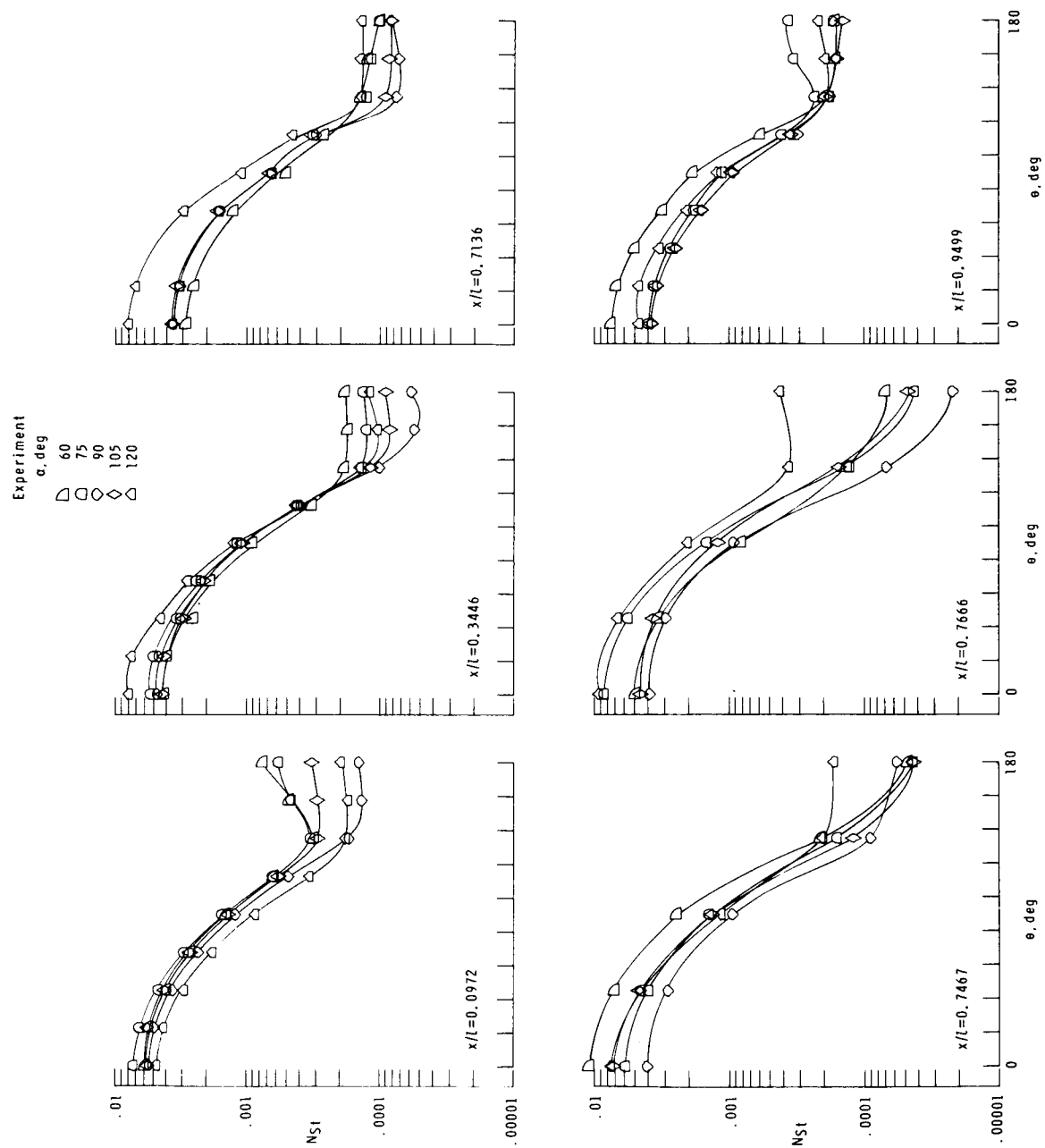
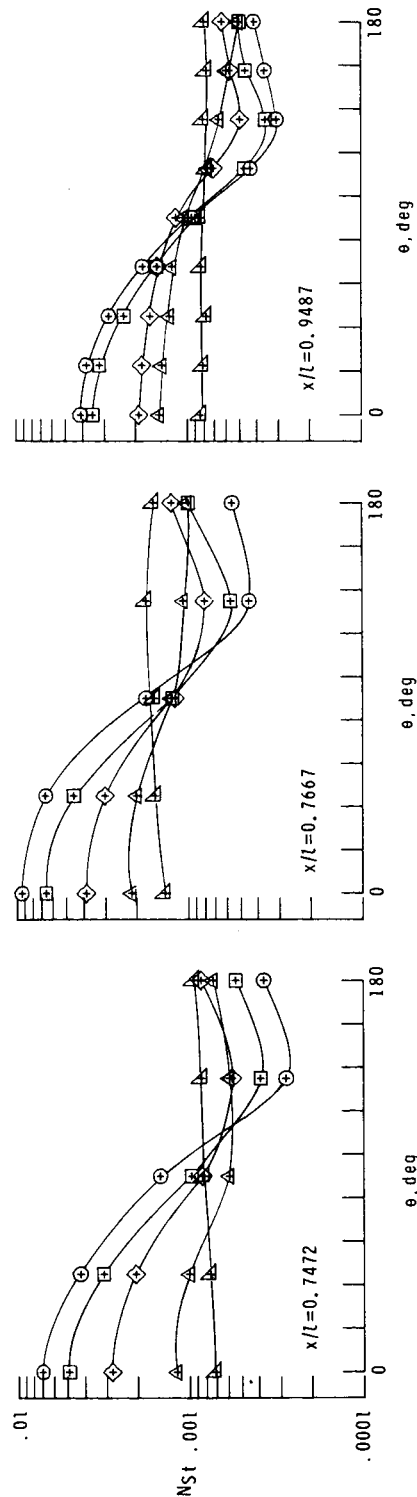
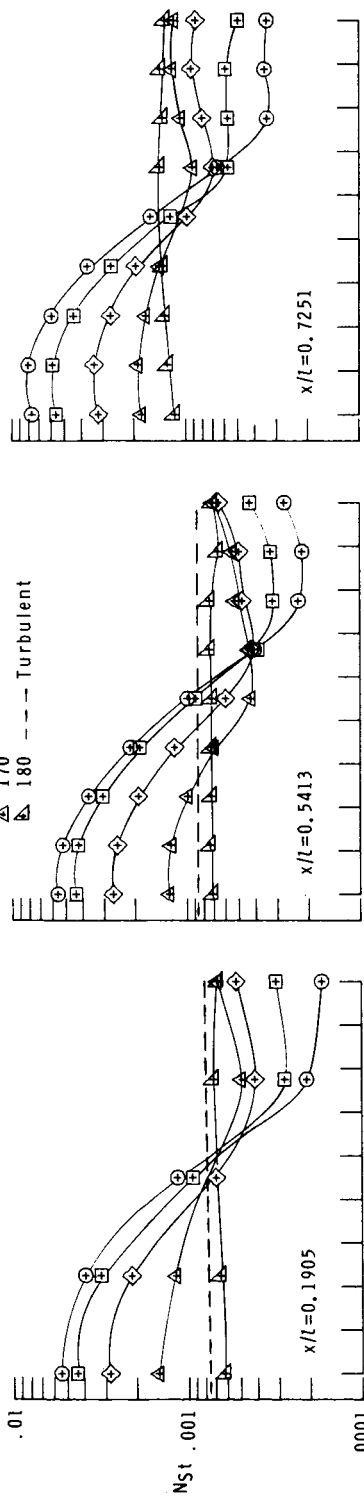


Figure 7.- Continued.

Experiment Theory, stagnation line

$\alpha$ , deg

$\oplus$  140  
 $\square$  150  
 $\diamond$  160  
 $\triangle$  170  
 $\triangle$  180 --- Turbulent



(c) Model C.

Figure 7.- Concluded.